

Reconstructions for continuous-wave diffuse optical tomography by a globally convergent method

Yueming Liu,¹ Jianzhong Su,^{1,*} Zi-Jing Lin,²
Steven Teng,¹ Aubrey Rhoden,¹ Natee Pantong,¹ and Hanli Liu²

¹Department of Mathematics, University of Texas at Arlington, Arlington, Texas 76019, USA

²Department of Bioengineering, University of Texas at Arlington, Arlington, Texas 76019, USA

*e-mail:su@uta.edu

Abstract: In this paper, a novel reconstruction method is presented for Near Infrared (NIR) 2-D imaging to recover optical absorption coefficients from laboratory phantom data. The main body of this work validates a new generation of highly efficient reconstruction algorithms called “Globally Convergent Method” (GCM) based upon actual measurements taken from brain-shape phantoms. It has been demonstrated in earlier studies using computer-simulated data that this type of reconstructions is highly efficient and stable for imaging complex distributions of optical absorption. The results in this paper demonstrate the excellent capability of GCM in working well with experimental data measured from optical phantoms mimicking a rat brain with stroke.

©2012 Optical Society of America

OCIS codes: (100.3190) Inverse problems; (000.4430) Numerical approximation and analysis; (110.6960) Tomography; (110.7050) Turbid media; (170.3880) Medical and biological imaging.

References and links

1. S. Srinivasan, B. W. Pogue, B. Brooksby, S. Jiang, H. Dehghani, C. Kogel, S. P. Poplack and K. D. Paulsen, “Near-infrared characterization of breast tumors in vivo using spectrally-constrained reconstruction”, *Technol. Cancer Res. T.*, **4**(5), 513-526 (2005).
2. C. Schmitz, D. Klemer, R. Hardin, M. Katz, Y. Pei, H. Graber, M. Levin, R. Levina, N. Franco, W. Solomon, and R. Barbour, “Design and implementation of dynamic near-infrared optical tomographic imaging instrumentation for simultaneous dual-breast measurements”, *Appl. Opt.*, **44**, 2140-2153 (2005).
3. Y. Xu, X. Gu, L. Fajardo, and H. Jiang, “In vivo breast imaging with diffuse optical tomography based on higher-order diffusion equations”, *Appl. Opt.*, **42**, 3163-3169 (2003).
4. A. Godavarty, A.B. Thompson, R. Roy, M. Gurfinkel, M.J. Eppstein, C. Zhang and E.M. Sevick-Muraka, “Diagnostic of breast cancer using fluorescence-enhanced optical tomography: phantom studies”, *J. Biomed. Opt.*, **9**(3), 488-496 (2004).
5. S. Gopinath, C. S. Robertson, R. G. Grossman, and B. Chance, “Near-infrared spectroscopic localization of intracranial hematomas”, *J. Neurosurg.*, **79**, 43-47 (1993).
6. A.Y. Bluestone, M. Stewart, J. Lasker, G.S. Abdoulaev and A.H. Hielscher, “Three-dimensional optical tomographic brain imaging in small animals, part I: hypercapnia”, *J. Biomed. Opt.*, **9**(5), 1046-1062 (2004).
7. G. Zhang, A. Katz, R.R. Alfano, A.D. Kofinas, P.G. Stubblefield, W. Rosenfeld, D. Beyer, D. Maulik, and M.R. Stankovic, “Brain perfusion monitoring with frequency-domain and continuous-wave near-infrared spectroscopy: a cross-correlation study in newborn piglets”, *Phys. Med. Biol.*, **45**, 3143-3158 (2000).
8. A.G. Yodh and D. A. Boas, “Functional imaging with diffusing light”, in *Biomedical Photonics Handbook*, T. Vo-Dinh, ed. (CRC Press, New York), 21-1 – 21-45 (2003).
9. D. K. Joseph, T. J. Huppert, M. A. Franceschini, and D. A. Boas, “Diffuse optical tomography system to image brain activation with improved spatial resolution and validation with functional magnetic resonance imaging”, *Appl. Opt.*, **45**: 8142-8151 (2006).
10. D. A. Boas, T. Gaudette, G. Strangman, X. Cheng, J. J. A. Marota, and J. B. Mandeville, “The accuracy of near infrared spectroscopy and imaging during focal changes in cerebral hemodynamics”, *NeuroImage*, **13**, 76-90 (2001).
11. B. Chance, E. Anday, S. Nioka, S. Zhou, L. Hong, K. Worden, C. Li, T. Murray, Y. Ovetsky, D. Pidikiti, and R. Thomas, “A novel method for fast imaging of brain function, non-invasively, with light”, *Optics Express*, **2**(10): 411-423 (1998).

12. D. A. Boas, T. Gaudette, G. Strangman, X. Cheng, J. J. A. Marota, and J. B. Mandeville, "The accuracy of near infrared spectroscopy and imaging during focal changes in cerebral hemodynamics", *NeuroImage*, **13**: 76-90 (2001).
13. K. K Wang and T.C. Zhu, "Reconstruction of in-vivo optical properties for human prostate using interstitial diffuse optical tomography", *Optics Express*, Vol. **17**, Issue 14, pp. 11665-11672 (2009)
14. T. O. McBride, B. W. Pogue, S. Jiang, U. L. Österberg, and K. D. Paulsen, "Initial studies of in vivo absorbing and scattering heterogeneity in near-infrared tomographic breast imaging", *Opt. Lett.*, **26**, 822-824 (2001).
15. V. Kolehmainen, S. Prince, S.R. Arridge and J. P. Kaipio, "A state estimation approach to non-stationary optical tomography problem", *J. Opt. Soc. Am. A*, **20**, 876-84 (2000).
16. Q. Zhang, D H Brooks and D A Boas, "A haemodynamic response function model in spatio-temporal diffuse optical tomography", *Phys. Med. Biol.*, **50**, 4625-44 (2005).
17. F. Irani, S. M. Platek, S. Bunce, A. C. Ruocco and D. Chute, "Functional near infrared spectroscopy (fNIRS): An emerging neuroimaging technology with important applications for the study of brain disorders", *Clin Neuropsychol* **21**, pp. 9-37 (2007).
18. D. R. Leff, F. Orihuela-Espina, C. E. Elwell, T. Athanasiou, D. T. Delpy, A. W. Darzi and G-Z Yang, "Assessment of the cerebral cortex during motor task behaviours in adults: A systematic review of functional near infrared spectroscopy (fNIRS) studies", *NeuroImage*, **54**, pp. 2922-2936 (2011).
19. F. Tian, M. R. Delgado, S. Dhamne, B. Khan, G. Alexandrakis, M. I. Romero, L. Smith, D. Reid, N. J. Clegg, and Hanli Liu, "Quantification of diffuse optical tomography for cortical reorganization in children with cerebral palsy", *Optics Express* **18**(25), 25973- 25986 (2010).
20. X. Cui, S. Bray, D. M. Bryant, G. H. Glover and A. L. Reiss, "A quantitative comparison of NIRS and fMRI across multiple cognitive tasks", *NeuroImage* **54**, pp. 2808-2821 (2011).
21. S. R. Arridge and J. C Schotland, "Optical tomography: forward and inverse problems", *Inverse Probl.*, **25**, 123010 (2009)
22. S. R. Arridge and J. C. Hebden, "Optical imaging in medicine: II. Modeling and reconstruction", *Phys. Med. Boil.*, **42**, pp. 841-853 (1997).
23. A. H. Hielscher, A. D. Klose and K. M. Hanson, "Gradient-based iterative reconstruction scheme for time-resolved optical tomography", *IEEE Trans. Med. Img.*, **18**, 262-271 (1999).
24. J. C. Schotland, "Continuous-wave diffusion imaging", *J. Opt. Soc. Am.*, **14**, 275-279 (1997).
25. M. A. O'Leary, D. A. Boas, B. Chance and A. G. Yodh, "Experimental images of heterogeneous turbid media by frequency-domain diffusion-photon tomography", *Opt. Lett.*, **20**, 426-428 (1995).
26. Y. A. Gryazin, M.V. Klibanov and T.R. Lucas, "Numerical solution of a subsurface imaging inverse problem", *SIAM J. Appl. Math.*, **62**, 664-683 (2001).
27. M. V. Klibanov and A. Timonov, *Carleman Estimates for Coefficient Inverse Problems and Numerical Applications*, (Brill Academic Publishers, VSP, Imprint Brill, Utrecht, Boston, 2004).
28. K. Lee, V. Markel, A.G. Yodh, S. Konecky, G.Y. Panasyuk and J.C. Schotland, "Imaging complex structures with diffuse light", *Opt. Express* **16**, 5048-5060 (2008)
29. M.V. Klibanov and A. Timonov, "Numerical studies on the globally convergent convexification algorithm in 2D", *Inverse Probl.*, **23**, 123-138 (2007).
30. H.B. Keller and D.J. Perozzi, "Fast seismic ray tracing", *SIAM J. Appl. Math.* **43**, 981-992 (1983).
31. J. Su, H. Shan, H. Liu and M.V. Klibanov, "Reconstruction method with data from a multiple-site continuous-wave source for three-dimensional optical tomography", *J. Opt. Soc. Am. A*, **23**, 2388-2395 (2006).
32. H. Shan, M. V. Klibanov, H. Liu, N. Pantong and J. Su, "Numerical implementation of the convexification algorithm for an optical diffusion tomograph", *Inverse Probl.*, **24**, 025006 (2008).
33. H. Shan, M. V. Klibanov, J. Su, N. Pantong and H. Liu, "A Globally Accelerated Numerical Method For Optical Tomography With Continuous Wave Source", *J. Inverse Ill-Posed Probl.*, **16**(8), 763-790 (2008).
34. L. Beilina and M.V. Klibanov, "A globally convergent numerical method for a coefficient inverse problem", *SIAM J. Sci. Comp.* **31**, 478-509, (2008).
35. L. Beilina and M.V. Klibanov, *Approximate Global Convergence and Adaptivity for Coefficient Inverse Problems*, Springer, New York, 2012.
36. J. Su, M.V. Klibanov, Y. Liu, Z. Lin, N. Pantong and H. Liu, "Optical imaging of phantoms from real data by an approximately globally convergent inverse algorithm", *Inverse Prob. Sci. Eng.*, available electronically at iFirst, 1-26, 2012; to appear in this journal.
37. N. Pantong, J. Su, H. Shan, M.V. Klibanov and H. Liu, "A Globally Accelerated Reconstruction Algorithm for Diffusion Tomography with Continuous-Wave Source in Arbitrary Convex Shape Domain", *J. Opt. Soc. Am. A*, **26**, 456-472, (2009).
38. M.V. Klibanov, J. Su, N. Pantong, H. Shan and H. Liu, "A globally convergent numerical method for an inverse elliptic problem of optical tomography", *Applicable Analysis*, **6**, 861-891, (2010).
39. Z-J Lin, H. Niu, and H. Liu, "Volumetric diffuse optical tomography for small animals using a CCD-camera-based imaging system", *Int. J. Optics*, in press (2011).
40. D. Isaacson, J.L. Mueller, J.C. Newell and S. Siltanen, "Reconstructions of chest phantoms by the D-bar method for electrical impedance tomography", *IEEE Trans. Med. Imaging*, **23**, 821-828, (2004).

41. H. Niu, F. Tian, Z. Lin and H. Liu, "Development of a compensation algorithm for accurate depth localization in diffuse optical tomography", *Opt. Lett.* **35**, 429-431 (2010).
 42. H. Niu, Z. Lin, F. Tian, S. Dhamne and H. Liu, "Comprehensive investigation of three-dimensional diffuse optical tomography with depth compensation algorithm", *J. Biomed. Opt.* **15**(4), 046005 (2010).
 43. T. J. Huppert, S. G. Diamond, M. A. Franceschini and D. A. Boas "HomER: a review of timeseries analysis methods for near-infrared spectroscopy of the brain", *Appl Opt* **48**: D280-D298 (2009).
 44. S. R. Arridge and W. R. B Lionheart, "Nonuniqueness in diffusion-based optical tomography", *Opt. Lett.*, Vol. **23**, No. 11, 882-884 (1998).
-

1. Introduction

The studies using Near Infrared light (NIR) for biomedical imaging have become quite extensive in the past 15-20 years. Earlier applications of NIR imaging started with breast imaging, see [1-4], since NIR has better penetration depths in soft tissues than visible light. Applications of NIR technologies have made tremendous progress, including the detection of brain injury/trauma, see [5], the determination of cerebrovascular hemodynamics and oxygenation, see [6-9], and functional brain imaging in response to a variety of neurological activations [10-12]. Recently, the technique was also successfully used for measuring the efficacy of photodynamic therapy for prostate cancer, see [13]. Among several common NIR imaging mechanisms Frequency Domain (FD) imagers were developed and used in patients, see [14], and Time Domain (TD) methods were used for brain studies in [15, 16]. As a low-cost alternative to the TD and FD imaging systems continuous-wave (CW) NIR imaging systems have become more commonly used in recent years. We refer interested readers to review the references [17-20] for further reading of functional NIR brain studies.

To spatially quantify brain hemodynamic activities resulting from functional neuronal signals, it is desirable to extract distributions of light absorption from light intensity measurements through mathematical models. Since these optical properties are described by coefficients in the light diffusion model, see [21, 22], one needs to solve an inverse problem of the corresponding partial differential equation, the diffusion equation, to obtain diffuse optical tomography (DOT).

The inverse reconstruction for DOT has been mathematically challenging. The problem is nonlinear as well as ill-posed. As reviewed by Hielscher in [23], the majority of the inverse reconstruction algorithms used for DOT has utilized a perturbation approach involving the inversion of large Jacobian matrices, for examples see [24-26]. A common point of these mathematical schemes is the trial and error procedure in searching a reasonable approximation of the solution of the problem. Because DOT problem is ill-posed and under-determined by its nature, one may utilize a regularization scheme to approximate the solution. With regularization introduced in solving the problem, more than one local minima of residue function exist in general. The successful reconstruction of the unknown coefficients depends highly on the initial guess being close to the true solution. In other words, because the least-square residues might have multiple local minima, see [27], the reconstruction may converge to a false solution (a different local minimum of the residue than the actual solution) if the initial point fails into its domain of attraction. One recent major advance in the field was done by Schotland and his collaborators using linearized equations to reconstruct see [28]. They were able to reconstruct in high resolution 3D NIR images without the use of iterative methods. Since their method is based on linear integral equations with explicit Green's functions, they overcame the shortcoming of local methods and achieved precise solutions. However their phantom experiments used a large number of measurement points (3×10^8) for a single experiment. Their mathematical approach was very different from our method which is a fully nonlinear model.

Our current focus of theoretical research is on numerical methods that have no restrictions on the initial guess, namely, the development of a Globally Convergent Method (GCM) as initiated by Klivanov and Timonov [27, 29]. Our earlier generation of a GCM is called a "convexification method," as introduced in [29], based on modified residual error estimates. A

typical Carleman weight function is an exponential function that weights more on the light source side, and the decay coefficient needs to be chosen according to the problem to modify the second derivative of the error function. When a proper Carleman weight function is added to the error terms, those residues depend on the unknown variable in a convex manner. Since any convex function is known to attain its unique minimum mathematically, the modified problem is assured to have the global convergence to the unique minimizer, and the solution can be obtained by solving the “weight-modified” inverse problem from any initial guess. Our current approach (2nd generation of a GCM) is called a continuation method or homotopy method, as defined in [30]. The homotopy connects the sought system with a similar system that is easier to solve. In this approach, our inverse reconstruction is a continuation of reconstructions from a DOT problem where light sources are far away yielding a “tail function”, see [31, 32] for references to the “tail function”. This new generation method has achieved satisfactory results in reconstructions of simulated CW data, see [33]. A similar GCM was developed for the case of the reconstruction of a coefficient in a wave-like time dependent partial differential equation by Beilina and Klivanov [34, 35]. This paper proceeds to show the validity of this method based on physical measurements using laboratory optical phantoms with the shape of a rat head. The recovered parameters include the locations and imaging contrasts of unknown inclusions hidden within the phantoms. Comparing with [36], the current paper reports the validation of GCM by reconstructing from the so called “Blind” data, i.e., reconstructing without assuming any prior knowledge of the total numbers, locations and the optical parameter values of inclusions. This is the main contribution of the paper to the DOT research community.

In this article we present the theory underlying the 2nd generation GCM in section 2. Section 3 presents the experimental setup for the optical phantom study and its data acquisition scheme in 3-D geometry to be processed for 2-D tomography. In section 4 we describe the numerical reconstruction steps and then present results of reconstructed absorption coefficients. We summarize by conclusions and discussions in section 5, in particular, compare GCM with a conventional DOT method which indicates the advantage of GCM in reconstructing the absolute values of inclusion absorption coefficients.

2. The mathematical model

2.1. The optical diffusion model

An optical light source can be used in three forms in DOT: (1) the light is amplitude-modulated at a radio frequency (RF) in Frequency-Domain NIR imaging, (2) the light has a short pulse with a pulse width of a few pico-seconds used in Time-Domain NIR imaging, and (3) the light has a continuous-wave (CW) form and the amplitude is independent of time. In this paper we only discuss the CW-based problem. The time-independent diffusion equation and boundary conditions of the CW case can be found in [21] for a source location parameter s :

$$\nabla \cdot (D(x, y) \nabla \Phi(x, y, s)) - \mu_a(x, y) \Phi(x, y, s) = -\delta(x - x_m, y - s), \quad (x, y) \in \Omega_0, \quad (1a)$$

$$\frac{\partial \Phi(x, y, s)}{\partial n} + \Phi(x, y, s) = 0, \quad (x, y) \in \partial\Omega_0, \quad (1b)$$

where $D = 1/(3\mu'_s)$. μ_a and μ'_s are the absorption and reduced scattering coefficients in the tissue, respectively, and $\Phi(x, y, s)$ is the photon fluence rate or photon density. The locations of the light sources (x_m, s) can be chosen at several points by varying s . For 2-dimensional inverse problem of Eq. (1), the source is modeled by a Dirac function in the domain Ω_0 in the same 2-dimensional plane. The forward problem domain Ω_0 should in theory be the entire 2-dimensional plane, but in calculation it is a truncated rectangle, see [35]. We call Ω_0 the background domain throughout this paper. Equation (1b) is commonly known as Robin Boundary condition, see [21].

Note that in our problem, $\mu_a(x, y)$ is the major unknown to be reconstructed. The optical absorption coefficient $\mu_a(x, y)$ is closely related to oxygenated (HbO) and deoxygenated (HbR) hemoglobin concentrations. Specifically, the determination of $\mu_a(x, y)$ at two wavelengths leads to the quantification of HbO, HbR, and total hemoglobin concentrations, see [16-20]. The total hemoglobin concentration is proportional to total blood volume, an useful physiological indicator. Thus $\mu_a(x, y)$ is an important index for imaging in functional brain research.

In real applications, the domain of interest is a bounded and irregularly shaped domain contained in the background domain Ω_0 . We call it the physical domain and write it as Ω , e.g. the cross section of a rat brain. The distribution of the absorption parameter $\mu_a(x, y)$ is unknown in the physical domain Ω . The locations of the light sources are outside of the physical domain Ω . When the forward problem (1) is restricted into the physical domain Ω we have

$$\nabla \cdot (D(x, y) \nabla \Phi(x, y, s)) - \mu_a(x, y) \Phi(x, y, s) = 0, \quad (x, y) \in \Omega, \quad (2a)$$

$$\Phi(x, y, s) = \varphi(x, y, s), \quad (x, y) \in \partial\Omega, \quad (2b)$$

where $\varphi(x, y, s), (x, y) \in \partial\Omega$ represents the light intensities that can be measured on the boundary of domain Ω . The right hand side of (2a) is equal to 0 because the light sources are located outside of the physical domain Ω and the light source is reflected in Eq. (2b).

We make a change of variable from $\Phi(x, y, s)$ to $\tilde{\Phi}(x, y, s)$ by letting $\tilde{\Phi}(x, y, s) = \Phi(x, y, s) \sqrt{D(x, y)}$. Then Eq. (2) becomes

$$\Delta \tilde{\Phi}(x, y, s) - a(x, y) \tilde{\Phi}(x, y, s) = 0, \quad (x, y) \in \Omega, \quad (3a)$$

$$\tilde{\Phi}(x, y, s) = \tilde{\varphi}(x, y, s), \quad (x, y) \in \partial\Omega, \quad (3b)$$

where $\tilde{\varphi}(x, y, s) = \varphi(x, y, s) \sqrt{D(x, y)}$ on the boundary of Ω and $a(x, y)$ is a new unknown coefficient, defined as:

$$a(x, y) = \frac{1}{2} \Delta (\ln D(x, y)) + \frac{1}{4} \nabla (\ln D(x, y)) \cdot \nabla (\ln D(x, y)) + \frac{\mu_a(x, y)}{D(x, y)}, \quad (4)$$

where Δ represents the Laplacian operator.

For the rest of this paper the focus is on the reconstruction of the parameter distribution $a(x, y)$. This parameter $a(x, y)$ reflects both the light absorption and the reduced scattering coefficients with a unit of cm^{-2} . In NIR CW modality, one cannot separate scattering coefficient and absorption coefficient in a single CW measurement [44]. Additional measurement in a different wave-length is needed, but that is more challenging in experiments. In practical NIR applications, especially for brain stroke studies, one chooses a NIR wave-length that is not very sensitive to scattering changes. We only study the absorption coefficient that is related to oxygenated (HbO) and deoxygenated (HbR) hemoglobin concentrations in the blood. Under this assumption, we only reconstruct the absorption coefficient, by assuming the scattering coefficient is known. When the scattering coefficient $\mu'_s(x, y) = \mu'_s$ is uniform in space, the unknown coefficient reduces to $a(x, y) = \mu_a(x, y) / D = 3\mu'_s \mu_a(x, y)$. The Influence of inhomogeneity and discrepancy of scattering coefficient will be discussed in the last section.

2.2. The idea of reconstruction

If $\tilde{\Phi}(x, y, s)$ is known in the whole physical domain Ω we can compute the coefficient $a(x, y)$ in Eq. (3) in a straightforward way by computing the second order derivative of $\tilde{\Phi}(x, y, s)$. A better and more stable solution, see [31], which involves only the first order derivative of $\tilde{\Phi}(x, y, s)$ utilizes a finite element version of Eq. (3)

$$\iint_{\Omega} \nabla \eta \cdot \nabla \tilde{\Phi}(x, y, s) - a(x, y) \tilde{\Phi}(x, y, s) \eta dx dy = 0, \quad (5)$$

where η is taken as any quadratic finite element function.

However, we only know $\tilde{\Phi}(x, y, s)$ on the boundary of Ω in real applications. So the idea of the reconstruction for the coefficient $a(x, y)$ is to construct an approximation of $\tilde{\Phi}(x, y, s)$ in the whole physical domain Ω from the boundary measurement data. In order to achieve this goal, a sequence of transformations of Eq. (3) is performed. The transformed equation can be solved in a regular domain, e.g. a rectangle domain which contains the physical domain Ω , see [37] for an example. Once we have an approximation of $\tilde{\Phi}(x, y, s)$, we use Eq. (5) to compute the coefficient $a(x, y)$.

2.3. Transformations

The first transformation is to let $u = \ln \tilde{\Phi}(x, y, s)$. Then Eq. (3a) becomes the nonlinear elliptic equation

$$\Delta u(x, y, s) + \nabla u(x, y, s) \cdot \nabla u(x, y, s) - a(x, y) = 0. \quad (6)$$

Recall that (x_m, s) are the locations of the light sources. The second transformation is to let $v = u / s^2$, and we obtain from Eq. (6) that

$$\Delta v + s^2 |\nabla v|^2 = \frac{a(x, y)}{s^2}. \quad (7)$$

By letting $q(x, y, s) = \partial_s v(x, y, s)$ be the changes of $v(x, y, s)$ with respect to the location of the light source we obtain the following nonlinear integral differential equation.

$$\Delta q + 2s^2 \nabla q \nabla v + 2s |\nabla v|^2 = -2 \frac{a(x, y)}{s^3}, \quad (8)$$

where

$$v(x, y, s) = -\int_s^{\bar{s}} q(x, y, \tau) d\tau + T(x, y), \quad s \in [s, \bar{s}]. \quad (9)$$

The term $T(x, y)$ is the so-called "tail function" and is defined to be $T(x, y) = v(x, y, \bar{s})$. By using Eq. (7) again to eliminate $a(x, y)$ on the right hand side of Eq. (8) and substituting Eq. (9) into Eq. (8), we obtain

$$\begin{aligned} \Delta q - \frac{2}{s} \int_s^{\bar{s}} \Delta q(x, y, \tau) d\tau - 2s^2 \nabla q(x, y, \tau) d\tau \\ + 4s \left(-\int_s^{\bar{s}} \nabla q(x, y, \tau) d\tau + \nabla T \right)^2 + 2s^2 \nabla T \cdot \nabla q = -\frac{2}{s} \Delta T. \end{aligned} \quad (10)$$

This is an integral-differential equation without the unknown coefficient $a(x, y)$. If we are able to approximate well both functions T and q , and their derivatives, then we can approximate well the target coefficient $a(x, y)$ via Eq. (5). We use the asymptotic relation in Section 2.4 to approximate $T(x, y)$ and then solve a discrete version of Eq. (10) to solve the problem. For the details of the algorithm, we refer to [38].

2.4. Asymptotic behavior

The constructed approximation of T is called ‘‘asymptotic tail’’. We outline the method below and refer the reader to [36] for its derivations.

We consider the asymptotic behavior of a solution $u(x, y, s)$ of Eq. (6) as $s \rightarrow \infty$. Assume that the value of function $a(x, y) = k^2 = \text{const} > 0$ outside of the domain Ω and s is large enough, then the approximation for $u(x, y, s)$ is

$$u(x, y, s) = -kS + \frac{1}{2} \ln \frac{\pi}{2S} + g(x, y) + O\left(\frac{1}{S}\right), \quad (11)$$

where the unknown function $g(x, y)$ is independent of the light source, as shown in [36]. Here $S(x, y, s) = |(x, y) - (x_m, s)|$ is the distance from the point (x, y) to the light source. To obtain $g(x, y)$, we first use light source s_1 and the measurement of $u(x, y, s)$ from the opposite boundary of Ω_1 at $x = x_0$ to get

$$u(x_0, y, s_1) = -kS(x_0, y, s_1) + \frac{1}{2} \ln \frac{\pi}{2S(x_0, y, s_1)} + g_1(x_0, y), \quad g_1(x, y) := g_1(x_0, y). \quad (12)$$

Then we apply the similar steps for other light source locations and the measurements are taken on the opposite side to get $g_2(x, y), g_3(x, y), g_4(x, y)$. Finally we obtain

$$g(x, y) = \frac{1}{4} \sum_{j=1}^4 g_j(x, y), \quad (13)$$

and an initial tail function

$$T(x, y) = -kS + \frac{1}{2} \ln \frac{\pi}{2S} + \frac{1}{4} \sum_{j=1}^4 g_j(x, y). \quad (14)$$

Once we have $T(x, y)$, we use an iterative scheme to improve contrasts of inclusions and to smooth out noises in boundary conditions. We skip the details; instead, we refer interested readers to reference [32, 36] for its acceleration property that helps the efficiency of reconstruction algorithms.

3. The phantom experiments

Our DOT imaging system is set for surface data collection and 3-D reconstruction through 2-D tomography of parallel cross-sections. The envisioned scenario is that of a rat brain which is covered with an optical mask that is filled with a ‘‘matching material’’, a gelatin tissue phantom that has similar optical properties to those of the rat’s skull/skin. The purpose of the experiment is to determine the unknown location and severity of a stroke in the rat brain phantom.

3.1 The measurement setup

Two optical phantoms are specifically designed and made for testing GCM-based imaging reconstructions, as a feasibility study for GCM applications in rat stroke models. The 3-D geometry of the phantoms is depicted in Fig. 1. Both phantoms are shaped as a hemisphere with a diameter of 13mm on top of a cube with dimensions 30 mm \times 30 mm \times 30 mm. The top hemisphere, the meshed shape in Fig. 1(a), mimics a rat head, and the cube of the phantom emulates an optical mask filled with the “matching material”. Spherical hollows of 2.5-3.0 mm diameter are within the phantoms. Fig. 2 shows horizontal cross-sections of the hemispheres of two different phantoms that were used in the experiments.

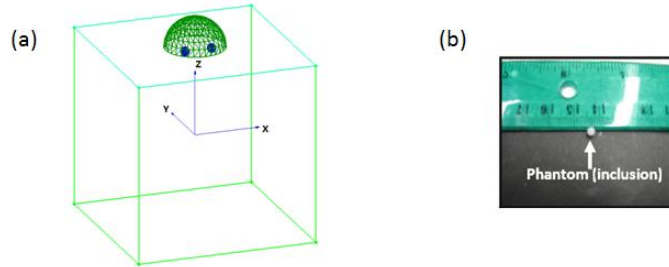


Fig. 1: (a) A schematic drawing for the 3-D geometry of an optical phantom. (b) A photograph of a spherical ink-intralipid gelatin phantom inclusion, shown with an actual ruler.

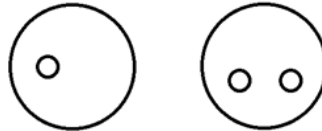


Fig. 2: Cross-sections of hemispheres in two different phantoms, with locations of inclusions marked by small circles. The left panel shows a cross section of the first phantom with one inclusion. The right panel shows a cross section of the second phantom with two inclusions.

The phantoms are made of gelatin mixed with the intralipid, a product for fat emulsion capable of mimicking light scattering in human or animal tissue when using light at wavelengths in the red and infrared ranges. The percentage of intralipid content is adjustable so that the phantoms can have the same optical parameters as the background medium of the target animal model. We fill the hollows with different spherical ink-intralipid mixed gelatin phantoms (Fig. 1(b)) acting as inclusions to model strokes due to blood clots.

Fig. 3(a) is a photo of the measurement setup. The center of the picture displays the optical phantom which contains the hidden inclusions that are not visible in the photo. The four thin tube-like probes are laser fibers that provide the light sources. A diode laser (Coherent Inc. wavelength at 808 nm) is multiplexed to serve as the source by a multiplexer (Avantes Inc. Multiplex Channels 1x16), which delivers and controls light at four locations through the four laser fibers. The fiber on the right-hand side of Fig. 3(a) can be moved to other positions by adjusting the mechanical arm that controls the lateral distance. A Charge-Coupled Device (CCD) camera for light intensity measurements is mounted directly above the setup (not shown in photo) where the camera focuses on the top surface of the phantom. The field of view (FOV) of the camera is 13 \times 11 mm². The CCD camera with its sensitivity and response range is commonly used for NIR imaging of animals. A schematic drawing of the experimental setup is shown in Fig. 3(b), and the procedures for calibration of the CCD camera can be found in [39].

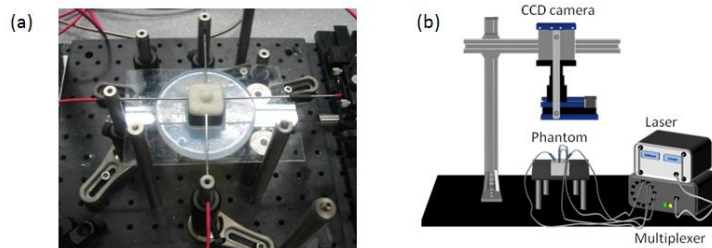


Fig. 3: (a) A photograph of the experimental setup (b) A 3-D schematic drawing of experimental setup for phantom study.

Because the said cross section is obstructed by the top surface of the hemisphere in the CCD's field of view, we can only collect the light intensity data at the boundary of a 2-D cross section of the presumed "animal head" as depicted in Fig. 4. The data extraction is done by an automated process as follow. 1) Export the data acquired by CCD camera (raw data format is exported by Matlab as a text file). 2) The light intensity at each of the grid points in the mesh is mapped into a matrix from the Matlab file. 3) Extract the light intensity data along the circle $\partial\Omega$, and the data set is used as the boundary condition φ .

The inverse reconstruction is performed in a 2-D plane, where the optical parameter distribution of the medium inside the circle (meshed area) is the unknown coefficient in the photon diffusion model. The 2-D tomographic treatment of the 3-D problem is similar to a successful treatment of experimental data in Electrical Impedance Tomography by a non-locally convergent algorithm in [40].

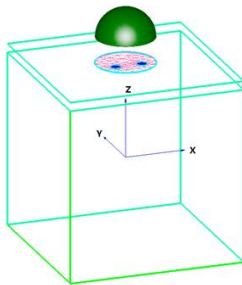


Fig. 4: A 3-D schematic drawing showing the data acquisition process of $\varphi(x, y, s)$ on the boundary of the physical domain Ω (meshed area) for Eq. (2b), from light intensity measurements of 3-D phantom surface by a CCD camera in experiments.

In our experiments the optical coefficients of the phantoms are $D = 1/(3\mu'_s) = 0.037$ cm uniformly, $\mu_a = 0.09$ cm⁻¹ for the background phantom (excluding the inclusions), and μ_a ranging from 0.18 to 0.4 cm⁻¹ for the inclusions by adjusting the ink-Intralipid mix. An inclusion with pure black ink has a theoretical value of μ_a that tends towards infinity. These optical parameters are standard values used for our rat brain phantom experiments.

The measurement procedure is straightforward. We follow a similar idea to that of frequency sounding, see [26, 34], but replace a changeable frequency with light sources located along a straight line. Our setting with 6 light source positions is adequate to obtain a reasonable reconstruction image. From previous tests with simulated data it was determined that more positions do not improve the quality of reconstructions significantly, see [37]. The relative convenience of the measurement procedure is one of the advantages of this method.

4. Reconstruction results

We describe the calibration of the parameters for numerical reconstruction in 4.1 and the results in 4.2. There are a number of ways to process the data, we refer to [38] for the pre-process procedure.

4.1 Calibrations

The optical properties of the phantom background without inclusions are known theoretically. However, there might be a discrepancy between the theoretical value and the actual measurement. Further, the scattering coefficient is also an important contributing factor in $a(x, y)$, and the result is sensitive to the discrepancy. We need to calibrate our model by adjusting the background value, k^2 , to match the experimental data measured with the reference background medium. First, we numerically solve the forward problem with the source position s_1 in the background domain Ω_0 without any inclusions,

$$\Delta\Phi - k^2\Phi = -A\delta(x - s_1, y - y_m), x \in \Omega_0, \quad (15)$$

where $k^2 = 3\mu_a\mu'_s$ is the background value. We calibrate the parameter μ_a (fixing μ'_s) as well as the amplitude $A > 0$ of the light source in Eq. (11) to match the experimentally measured light intensity. We choose A in such a way that $\Phi_{comp}(x_{max}, y_{max}, s_1) \approx \Phi_{meas}(x_{max}, y_{max}, s_1)$, where $\Phi_{comp}(x_{max}, y_{max}, s_1)$ and $\Phi_{meas}(x_{max}, y_{max}, s_1)$ are computed and measured light intensities, respectively. Here (x_{max}, y_{max}) is the brightest point, i.e., the farthest right point on $\partial\Omega$ being closest to the light source. Next, we approximate the constant k^2 . To do this, we take another sampling point (x_{min}, y_{min}) with the minimum light intensity which is the farthest left point on $\partial\Omega$. We consider the ratios $R_{comp}(k^2)$ and R_{meas} where

$$R_{comp}(k^2) = \frac{\Phi_{comp}(x_{max}, y_{max}, s_1)}{\Phi_{comp}(x_{min}, y_{min}, s_1)}, R_{meas} = \frac{\Phi_{meas}(x_{max}, y_{max}, s_1)}{\Phi_{meas}(x_{min}, y_{min}, s_1)}.$$

We chose k^2 such that $R_{comp}(k^2) \approx R_{meas}$. As a result, the calibrated value was $k^2 = 2.43$. This computed value matches quite well with the theoretical value of 2.4 for the intralipid solution we have used. For the case of small animal measurements we can use one standard intralipid for all samples. The calibration process for k^2 is used to determine the ‘‘average’’ background absorption value of the target domain.

4.2 ‘‘Blind data’’ test results from GCM reconstructions

The reconstruction is done without assuming any prior knowledge of the total number, location or optical parameter values of the inclusions. We collected six groups of ‘‘blind data’’ with inclusions and an additional group of measurement data for the phantom without any inclusion as the background reference. Within the six groups, the first three have one inclusion each of which has different absorption contrasts; see the left panel of Fig. 2. The last three groups have two inclusions; see the right panel of Fig. 2, also with three different contrasts.

Let $a_{incl} = \max_{(x,y)} a(x, y)$ be the peak value of the inclusion, and a_{bk} be the background value.

Then the contrasts in our experiments are $a_{incl} / a_{bk} = 2, 3$ and 4 , respectively.

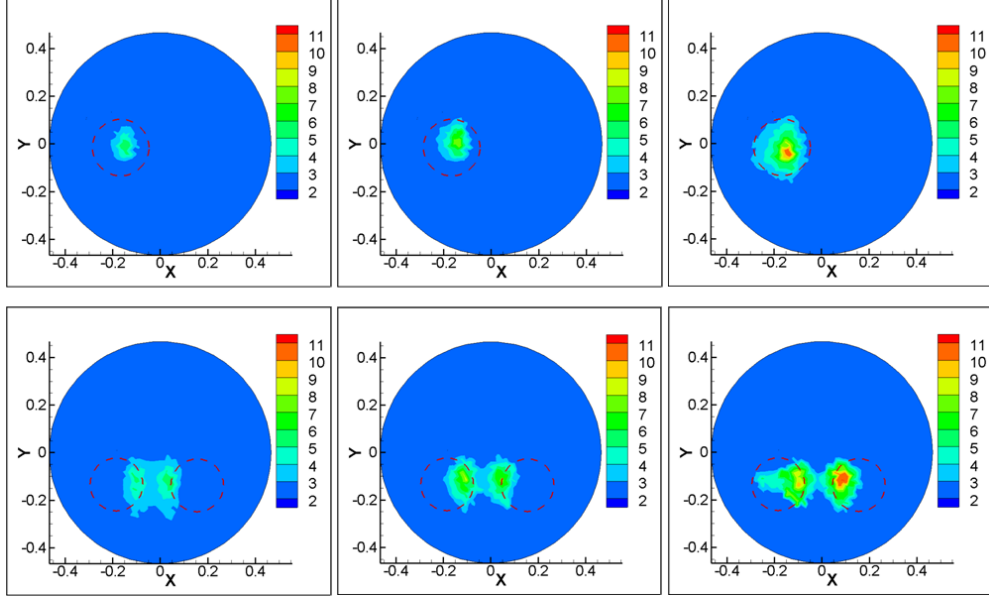


Fig. 5: Reconstructed $a(x,y)$ for the six groups of data. In the upper panel, actual distributions $a(x,y)$ have one inclusion, and in the lower panel, actual distributions $a(x,y)$ have two inclusions. The contrasts are arranged in the order 2:1, 3:1 and 4:1, from left to right. The locations of the actual inclusions are marked out in the dashed circles.

Fig. 5 shows the reconstructed images of all six groups of data. The recovered positions in the first three groups are within the circle of the actual position of the single inclusion, the dashed circle. The recovered positions in the last three groups are also approximate to the actual locations of the inclusions, the two dashed circles, except that the distance between the two reconstructed inclusions is closer than the actual distance. However, we observe from the lower panel of Fig.5 that the distance between two reconstructed inclusions becomes larger when the contrast of the inclusions increases (from left to right in the figure). Especially, in the figure of two inclusions with contrast 4:1, the lower right panel, the two inclusions can be better resolved from each other.

Listed in Table 1 are the maximal contrast values and relative errors for all six cases. It shows that we have imaged the contrast values of the inclusions in the same scale of magnitude. These contrast values are important as they can be further used to calculate HbO and HbR levels. In Table 2, we show the localization errors of our reconstructions. The absolute localization error is defined as the distance between the actual center C_{actual} and the center location C_{recon} of a reconstructed inclusion where $a(x,y)$ attains a maximal contrast value. The relative localization error is defined as $|C_{recon} - C_{actual}|/R$ where R is radius of Ω . We have observed that the localization errors tend to increase with an increase in the number of inclusions.

Table 1. Reconstructed maximal contrast values a_{incl} / a_{bk} within imaged inclusions and relative errors of $a(x,y)$ in terms of maximal contrast values.

Actual contrast (# of inclusions)	Reconstructed contrast	Relative Errors
2:1 (One inclusion)	2.33	16.7%

3:1 (One inclusion)	3.29	9.86%
4:1 (One inclusion)	4.57	14.3%
2:1 (Two inclusions)	2.29	14.8%
3:1 (Two inclusions)	3.49	16.4%
4:1 (Two inclusions)	4.58	14.7%

Table 2. Localization errors $|C_{recon} - C_{actual}|/R$ of reconstructed $a(x,y)$ by GCM method.

Actual contrast	One Inclusion		Two Inclusion			
			Left		Right	
2:1	0.50mm	5.3%	1.6mm	17.1%	2.4mm	25.6%
3:1	0.70mm	7.5%	1.7mm	18.2%	2.3mm	24.6%
4:1	0.60mm	6.4%	1.4mm	15.0%	1.3mm	13.9%

5. Conclusions and discussions

We have applied the GCM of [38] for a Coefficient Inverse Problem to DOT phantom measurements. These data mimic imaging of a blood clot in a rat brain. Reconstructions are performed without any prior knowledge of the inclusions. In our 6 cases, we found that reconstructed images of inclusions from NIR experimental data are quite accurate, including both locations of inclusions and inclusions-to-background contrasts. The main contribution of this paper is the validation of GCM by reconstructing from the so called ‘‘Blind’’ data, i.e., reconstructing without assuming any prior knowledge of the total numbers, locations and the optical parameter values of inclusions.

Our GCM compares favorably with other conventional locally convergent methods. We have tested the same data sets with a conventional DOT reconstruction method. The conventional DOT method was performed using a publicly available software HomER (<http://www.nmr.mgh.harvard.edu/PMI/resources/homer/home.htm>) [43], as used in [41, 42].

In Fig. 6, we show the reconstructed images by the conventional DOT reconstruction method for one-inclusion cases. The locally convergent method can identify the changes in the absorption coefficient well; however, note that the conventional DOT algorithm cannot reconstruct the absolute value of $a(x,y)$ due to the limitations of the method. The images in Fig. 6 depict $\Delta a(x,y)$, the change of the coefficient from the background in the range $[-5 \times 10^{-4}, 20 \times 10^{-4}]$, while the images in Fig. 5 depict $\Delta a(x,y)$ in the range $[1,10]$ which is in the same range as actual change.

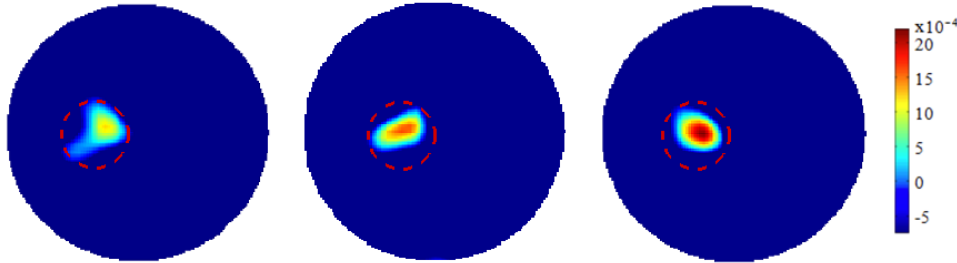


Fig. 6: Reconstructed results (changes of $a(x,y)$ from background) for the first three groups of data (single inclusion) by using the conventional DOT algorithm. The contrasts are similarly arranged in the same order as 2:1, 3:1 and 4:1 from left to right. Actual positions of inclusions are marked out by dashed circles.

Here we will briefly discuss the comparison of our phantom results with our early results in applying GCM to simulated data, see [37]. For a similar case with two inclusions with 3:1

contrast, the relative error in peak value was less than 15% for simulated data, while the relative error in peak value for phantom data is less than 17%. The relative localization errors are higher for the phantom studies, 3% (inclusion 1) and 12% (inclusion 2) for simulated data versus 18% and 24% for the phantom.

The errors are contributed by several factors, noise in experiments, numerical errors as well as the discrepancy of the mathematical model and experiments. An anonymous referee suggested that using a mix of intralipid and non-scattering absorbers might yield to a better comparison for the purpose of method validation, as this will exactly correspond to the mathematical model. We plan to implement this experimentally in our future study.

As stated in section 2, we focus on the reconstruction of the parameter distribution $a(x, y)$ which reflects both the light absorption and the reduced scattering coefficients. We assume the scattering coefficient $\mu'_s(x, y)$ is known and uniform in our experiments. Under this assumption, the unknown coefficient $a(x, y)$ in Eq. (4) reduces to $3\mu'_s\mu_a(x, y)$. We also assume that μ'_s keeps unchanged during the background measurements and measurements with inclusions. The reconstructed contrast a_{incl} / a_{bk} reflects the change in absorption coefficients $\mu_a(x, y)$. However, in application for small animal measurements the scattering coefficient is neither homogeneous or it remains unchanged with time. Further study based on an extensive number of numerical simulations was done to test applicability of the method to cases where scattering coefficient is in general not homogenous, changing with time, and unknown. The answer is favorable that GCM is capable of dealing with inhomogeneous scattering coefficient, or discrepancy and fluctuation in its values. In fact, the main advantage of GCM method is that it is independent of initial guess based on baseline scattering value, as iterations from any initial point are mathematically proven to converge to a true solution subject a margin of error.

In order to quantify the errors in recovered contrasts in $\mu_a(x, y)$ with respect to discrepancies in the assumed background scattering coefficient, numerical simulations has been done to provide the simulated data and to reconstruct. Three different error patterns have been studied, as shown in the upper panel of Fig. 7. The amount of errors in scattering coefficient ranges from -15.0% to 15.0%. The locations of the reconstructed inclusions are precise, where reconstructed inclusion patterns are similar to these of fig. 5. The reconstructed contrasts are shown in the lower panel of Fig. 7. The results show that the errors in the recovered contrasts in $\mu_a(x, y)$ are pretty accurate (less than 3.0%) for all the test cases.

We then studied the case where the scattering coefficient changes after the background measurements were done. Its purpose is to test the capability of the method in dealing with animal data where scattering coefficient fluctuate with time during experiments. The changes of scattering coefficients occur in locations where inclusions are at. The error pattern is the same as the one shown in the middle of the upper panel in Fig. 7. The reconstructions were also successful: the locations of the inclusions are precise. However the relative peak errors change with the magnitude of fluctuations in scattering coefficients. The recovered contrasts in $\mu_a(x, y)$ are shown in Fig. 8. It shows that in this case the errors in the recovered contrasts depend on the errors in the scattering coefficient linearly. The increasing of reconstruction errors is due to the sensitivity of the solution to the scattering coefficient variance.

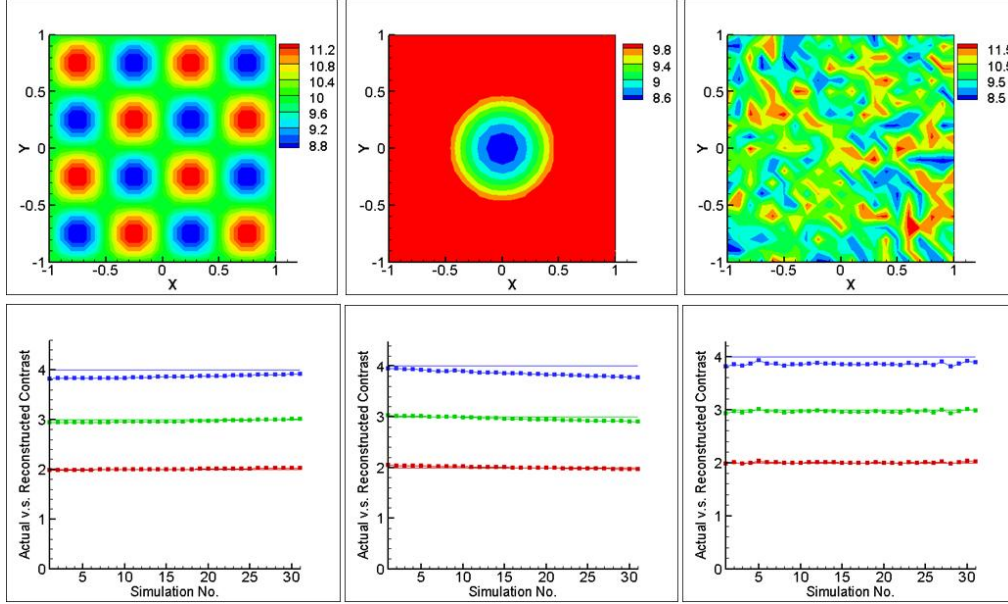


Fig. 7: In the upper panel, three typical error patterns in the background scattering coefficient are shown. In the lower panel, the recovered contrasts (lines with square symbols) and actual contrasts in $\mu_a(x, y)$ are shown in one figure for tests with contrasts 2, 3 and 4. In each case, 31 simulations are done with respect to the errors in the scattering coefficient that range from -15.0% to 15.0% with 1.0% step length.

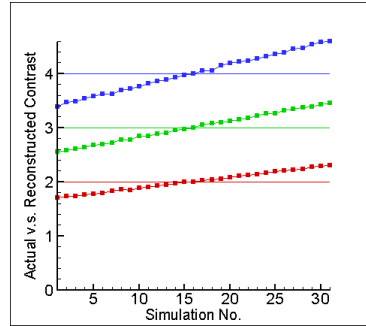


Fig. 8: The recovered contrasts (lines with square symbols) and actual contrasts in $\mu_a(x, y)$ in the cases of that the scattering coefficient changes after the background measurements

GCM is a rather robust numerical reconstruction algorithm, being able to deal with a wide range of inclusions. (This is because GCM is based on an approach to solve a system of elliptic partial differential equations (more similar to a forward problem), where numerical methods are quite mature for large-scale computations.) Therefore, the method can provide stable results when it gets utilized for large data sets of 512X512 output pixels from a CCD camera. Because of this unique property, we can deal with large data sets generated by several sources positions and have the capability to handle complex shapes using a large number of grid points, as shown in this paper. In contrary, a method that is not GCM will usually have increasing amounts of errors when the initial guess moves away from actual distribution, as shown in [31]. The computational times for both methods are similar, about 1-2 minutes [35].

In summary, we have validated our GCM reconstruction algorithm based on real data acquired by a NIR CCD Camera using optical phantoms after testing the GCM method on computer simulated data in [33, 37, 38]. This study has confirmed the ability of GCM to

reconstruct improved DOT images using laboratory rat-head phantoms. We will soon publish our results on the related inverse problems and their applications in actual animal studies.

Acknowledgements: The work of all authors was supported by the National Institutes of Health grant number No. 5R33CA101098.